ARMY RESEARCH LABORATORY

Emulation of Forward-looking Radar Technology for Threat Detection in Rough Terrain Environments: A Scattering and Imaging Study

by DaHan Liao and Traian Dogaru

ARL-TR-6312 **December 2012**

Approved for public release; distribution unlimited.

NOTICES

Disclaimers

Army Research Laboratory
Adelphi, MD 20783-1197

ARL-TR-6312 **December 2012**

Emulation of Forward-looking Radar Technology for Threat Detection in Rough Terrain Environments: A Scattering and Imaging Study

DaHan Liao and Traian Dogaru
Sensors and Electron Devices Directorate, ARL

REPORT DOCUMENTATION PAGE

Form Approved
OMB No. 0704-0188

1. REPORT DATE *(DD-MM-YYYY)*
December 2012

2. REPORT TYPE
Final

3. DATES COVERED (From - To)
2011–2012

4. TITLE AND SUBTITLE
Emulation of Forward-looking Radar Technology for Threat Detection in Rough Terrain Environments: A Scattering and Imaging Study

5a. CONTRACT NUMBER

5b. GRANT NUMBER

5c. PROGRAM ELEMENT NUMBER
1NE4II

6. AUTHOR(S)
DaHan Liao and Traian Dogaru

5d. PROJECT NUMBER

5e. TASK NUMBER

5f. WORK UNIT NUMBER

7. PERFORMING ORGANIZATION NAME(S) AND ADDRESS(ES)
U.S. Army Research Laboratory
ATTN: RDRL-SER-U
2800 Powder Mill Road
Adelphi MD 20783-1197

8. PERFORMING ORGANIZATION REPORT NUMBER
ARL-TR-6312

9. SPONSORING/MONITORING AGENCY NAME(S) AND ADDRESS(ES)

10. SPONSOR/MONITOR'S ACRONYM(S)

11. SPONSOR/MONITOR'S REPORT NUMBER(S)

12. DISTRIBUTION/AVAILABILITY STATEMENT
Approved for public release; distribution unlimited.

13. SUPPLEMENTARY NOTES

14. ABSTRACT

Large-scale, full-wave modeling of multi-static target imaging in a rough-ground environment is described. The emulation methodology employs a parallelized three-dimensional "near-field" finite-difference time-domain algorithm in characterizing the electromagnetic scattering from the ground-surface and buried and on-surface targets in the form of landmines and unexploded ordnances. Subsequent focusing of the scattered fields into an image is obtained with the time-reversal technique. The emphasis of this study is on investigating the detectability of discrete ground targets in the presence of distributed variable ground clutter as relevant to performance prediction for ultra-wideband forward-looking radar applications.

15. SUBJECT TERMS
Computational electromagnetic, ground-penetrating radar, rough terrain, target detection, time-reversal imaging

16. SECURITY CLASSIFICATION OF:			17. LIMITATION OF ABSTRACT	18. NUMBER OF PAGES	19a. NAME OF RESPONSIBLE PERSON
a. REPORT	b. ABSTRACT	c. THIS PAGE			DaHan Liao
Unclassified	Unclassified	Unclassified	UU	30	19b. TELEPHONE NUMBER (*Include area code*) (301) 394-1741

Standard Form 298 (Rev. 8/98)
Prescribed by ANSI Std. Z39.18

Contents

List of Figures

Acknowledgment

The Department of Defense (DoD) High Performance Computing (HPC) Modernization Program supported this project by supplying supercomputer time under the Computing Project C5C. The simulations were performed at the U.S. Army Research Laboratory DoD Supercomputing Resource Center at Aberdeen Proving Ground, MD.

INTENTIONALLY LEFT BLANK.

1. Introduction

Electromagnetic-oriented detection is expected to be an integral component of the U.S. Army's multi-sensor-based strategy for force protection and route clearance. Over the last decade, a myriad of research avenues have been directed toward developing ground-based, ultra-wideband (UWB) radars with the capability to simultaneously penetrate the ground, and image concealed landmines and improvised explosive devices (IEDs) from a standoff distance (Kositsky et al., 2002; Bradley et al., 2003; Wang et al., 2005; Ressler et al., 2007; Wang et al., 2008). Despite the fact that experimentation over the last several years has demonstrated the potential of the technology against certain classes of targets, the amorphous nature of the encountered threats has complicated the development and fielding of the technology. One promising system—developed at the U.S. Army Research Laboratory (ARL)—is the low-frequency, UWB synchronous impulse reconstruction (SIRE), imaging ground-penetrating radar (GPR) (figure 1), which is a vehicle-based platform operating at the nominal frequency band of 500–2500 MHz with the forward-looking coverage angle spanning approximately 5°–20° with respect to the horizon. As opposed to conventional downward-looking GPR, a forward-looking GPR such as the SIRE system offers the advantage of having a reduced ground-bounce return due to the use of a sensing geometry at an off-normal—or near-grazing—angle. One of the disadvantages of the forward-looking geometry is realized by first noting that the overall backscattered signal power response of a target, either on-surface or buried, decreases as a function of the illumination-angle approximately proportional to the form of $|(1+R(\theta_{illu}))|^4$, where $R(\theta_{illu})$ is the reflection coefficient of the ground-surface. (Here, it is assumed the predominant interactions are from plane-wave far-field effects—with negligible surface-wave contributions). This behavior of the scattering response makes the standoff detection of ground targets a challenge, especially when the targets are non-metallic and constraints may be imposed on the maximum power that the radar transmitter can radiate.

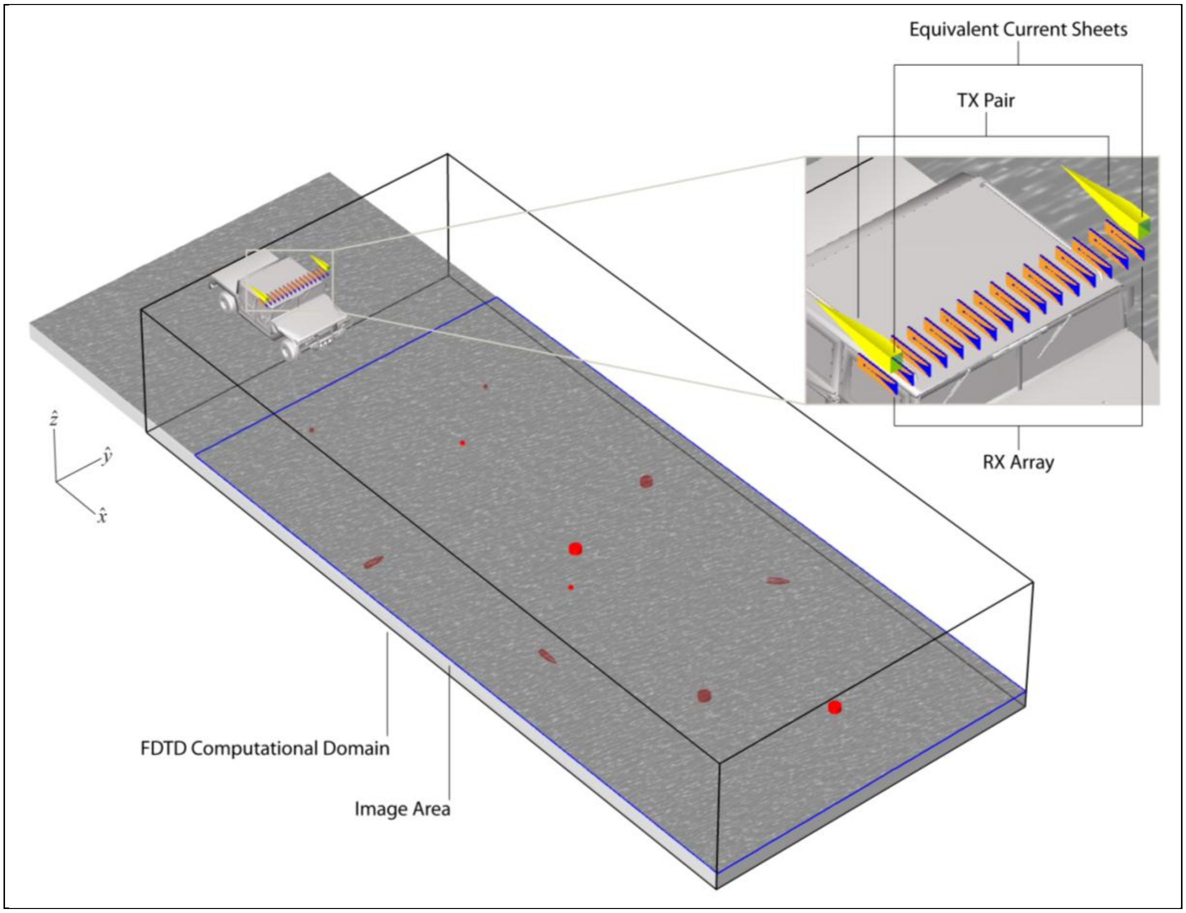

Figure 1. Simulation domain: forward-looking sensing of a terrain scene. Note that the vehicle, transmitting and receiving antennas are not included in the finite-difference time domain (FDTD) grid—the transmitting antennas are replaced with equivalent aperture current distributions, and the electric fields are simply sampled at the locations of the receiving antennas for image generation.

In general, as shown by Liao (2011) in a study focused mainly on landmines and metallic shells, the radar responses from shallow-buried targets are—depending on the polarization—at least 8 to 20 dB weaker than those from their on-surface counterparts and, hence, are much more vulnerable to interference scattering effects arising from interface roughness and subsurface clutter. As such, the understanding of the scattering responses of distributed and discrete ground clutter (e.g., surface unevenness, soil inhomogeneities, plant roots, and ground debris) is expected to play an important role in assessing the detectability limit of the radar for sensing buried targets. The scattering interactions within a radar scene, inherently, are intricate functions of the radar geometry (i.e., transmitter/receiver-to-target distance, array configuration), transmission and reception polarizations, frequency, as well as the electrical and physical properties of the targets and the terrain environment. From the electromagnetic perspective, in analyzing a low-to-ground system such as the SIRE radar, as the propagation paths defining the radiowave interactions between the radar transceiver and the targets adhere to the ground, existing analytical and heuristic ground-surface and target-scattering models often prove to be insufficient in characterizing various backscattering phenomena of interest. Accordingly, from the system development perspective, full-wave electromagnetic simulations are desired—and necessary—for an accurate prediction of the performance of the forward-looking radar.

Previous efforts in systematically modeling the operation of radio sensing technology for the detection of ground targets include the studies outlined by Bourgeois and Smith (1996); Bourgeois and Smith (1998); Teixeira et al. (1998); Gürel and Oğuz (2000); Gürel and Oğuz (2001); Lampe and Hooliger (2001); and Uduwawala et al. (2005)—albeit the focus of these works is mostly on the downward-looking sensing geometry, and thus the simulation domains considered therein are relatively small. In the work by Teixeira et al. (1998), a FDTD method is used for computing the scattering from metallic and plastic pipes buried in a ground with dispersive soil. To mitigate the direct signal coupling between the transmitter and receiver, in the work by Gürel and Oğuz (2000), the transmitting and receiving elements are housed in a shielding structure coated with absorbers; surface roughness and soil heterogeneities are also included in the model by populating random scatterers within the FDTD computational grid. In both studies above, the transmitters and receivers are assumed to be electric dipoles; UWB radiators more akin to those used in actual GPR systems are analyzed by Bourgeois and Smith (1996), Lampe and Hooliger (2001), and Uduwawala et al. (2005), where bow-tie antennas are exploited as sources of illumination. In all the aforementioned studies, the emphasis is on characterizing the ground and target-scattering responses, and therefore no imaging results are included. Note that in addition to FDTD techniques, many method-of-moments (MoM)-based approaches also have been proposed (He et al., 2000; El-Shenawee et al., 2001a; El-Shenawee et al., 2001b; Johnson and Burkholder, 2001; El-Shenawee and Rappaport, 2002; Johnson, 2002; Wang et al., 2003; Altuncu et al., 2006; Guan et al., 2009) to facilitate GPR-related numerical investigations—including cases where the ground-surface roughness needs to be taken into account; sensing and imaging at grazing-angles, however, are not discussed in detail within these works.

An effort by the authors to characterize the detection operation of the SIRE radar using a full-wave electromagnetic solver is documented in previous works (Liao et al., 2010; Liao and Dogaru, 2011a; Liao and Dogaru, 2011b; Liao and Dogaru, 2012), in which only far-field interactions are studied—that is, the excitation of the target and the environment is supplied by pure plane waves, and the receivers of the scattered signal are placed at infinity. In the current work, to achieve a more accurate emulation of the sensing operation employed by the SIRE radar, a "near-field" FDTD approach is proposed to provide system-level analysis, and for tracking the propagation and scattering of the radio-wave energy through the computational domain. This study takes advantage of the computing resources received through the three-year High Performance Computing Modernization Program Challenge Project award entitled "Advanced Computational Modeling of Forward-Looking Radar for the Detection of Landmines and IEDs." This report provides a summary of the works performed during the first year of the project and is organized as follows: section 2, the framework of the full-wave-based radar emulator is detailed; section 3, an investigation of the validity of the "near-field" FDTD algorithm is put forth; and section 4, a demonstration of the effects of ground clutter on target imaging generated by the time-reversal technique is presented with the simulation of a large terrain scene consisting of targets in a rough ground environment. In sum, this study illustrates the practicality of the chosen full-wave simulation strategy for the emulation of forward-looking radar operation and imaging.

2. Electromagnetic Simulation and Analysis Framework

In demonstrating the modeling framework put forth in this study, electromagnetic simulation and coherent imaging of the scene depicted in figure 1 is considered. Note that during in-field operations, the ARL SIRE radar integrates scattering responses gathered at multiple vehicle locations to form the final image for a scene. As this is the first phase of the numerical investigation, in order to establish a baseline for validation and identify any potential fundamental limitations of the solver, the radar transceiver is assumed to be fixed in position, with the image synthesized from return signals captured at only a single aperture. With these considerations, the components of the forward-looking radar emulation engine are outlined below.

2.1 Terrain Characterization

The ground is modeled as a non-dispersive, non-permeable homogeneous medium with effective relative dielectric constant ε_r and conductivity σ_d. The electrical properties of the ground are dependent upon the soil composition and moisture content; ε_r and σ_d can be either determined using direct dielectric measurement techniques or approximated with empirical-based formulations (Dobson et al., 1985; Peplilnski et al., 1995). The surface statistics of the ground, in general, are described by two functions: the probability density function of the height variations and the surface autocorrelation function. Within the scope of this study, a two-dimensional zero-mean surface profile obeying Gaussian statistics $\{h_{rms}, l_c\}$—where h_{rms} is the root mean square (rms) height and l_c the correlation length—is assumed and generated from its randomized power spectral density function by following the procedure prescribed by Thorsos (1988).

2.2 Ground Targets

As illustrated in figure 1, targets in the form of landmines (either anti-tank or anti-personnel, metallic or plastic, buried or on-surface) and 155-mm shells (metallic, buried) are considered. Specifically, these targets—the shapes, dimensions, orientations, and locations of which are also indicated by the white outlines in figure 4a—include the following: (1) Buried metallic anti-personnel landmine; (2) buried plastic (ε_r=3.1, σ_d=2 mS/m) anti-personnel landmine; (3) on-surface plastic (ε_r=3.1, σ_d=2 mS/m) anti-personnel landmine; (4) buried metallic 155-mm shell; (5) buried metallic anti-tank landmine; (6) on-surface metallic anti-tank landmine; (7) buried metallic 155-mm shell; (8) Buried metallic 155-mm shell; (9) On-surface metallic anti-personnel landmine; (10) buried plastic (ε_r=3.1, σ_d=2 mS/m) anti-tank landmine; and (11) on-surface plastic (ε_r=3.1, σ_d=2 mS/m) anti-tank landmine. Buried targets are positioned at 3 cm below the surface.

2.3 Transmitting and Receiving Antenna Treatment

The SIRE radar employs two transverse electromagnetic (TEM) horn antennas as transmitters and 16 Vivaldi antennas distributed over a 2 m-wide aperture as receivers. In the current implementation of the algorithm, the TEM horn transmitting antennas are simply replaced by equivalent current distributions; that is, the following electric and magnetic current sheets are positioned at the horn apertures (figure 1): $\vec{J} = \hat{x} \times \vec{H}$; $\vec{M} = \vec{E} \times \hat{x}$, where the electric and magnetic fields are assumed to be constant over the apertures. The Vivaldi antennas are not included in the FDTD model: the electric fields are sampled at the locations of the 16 antennas for image generation.

2.4 Three-dimensional “Near-Field” FDTD Algorithm

The composite scattering from the targets and the rough ground is calculated numerically with the FDTD method (Taflove and Hagness, 2005), which directly solves the differential forms of Maxwell’s equations in the spatial and temporal domains. In essence, the three-dimensional computational domain is decomposed into small cubic cells, with each cell assigned the material dielectric properties of the corresponding region in space. Electric and magnetic field components are sampled along the cells’ edges and faces, and the field spatial distribution is then propagated in time according to a time-marching scheme that implements a discretized version of Maxwell’s equations. The entire computational grid is terminated by a perfectly matched layer (PML) that emulates reflection-less propagation of the outgoing waves in infinite space. In the current application, an infinite half-space (air/ground layered media) is considered as the background environment in which the targets are embedded; the rough ground-surface is introduced as a finite, random perturbation of the flat interface between the two media (the approach is similar to that described by Liao and Dogaru [2012]). The overall FDTD code has been fully parallelized and runs on large distributed computer systems using the Message Passing Interface (MPI) framework: the computational domain is decomposed into rectangular sub-domains and the FDTD equations are solved separately for each sub-domain within one MPI process. Since only the electric and magnetic field samples in the boundary-layer between two adjacent sub-domains need to be exchanged between the respective processes, the code is highly scalable, even when the number of MPI processes is in the hundreds.

The field excitation sources in the algorithm are implemented as electric and magnetic current distributions in space (“soft sources”), which are added to the regular FDTD field update equations at the desired sample points. Note that by choosing this approach, direct, full-scale modeling of the transmitting antenna inside the FDTD code is avoided; instead, the antenna is replaced with electric and/or magnetic current distributions by employing the equivalence principle. Computation of these current distributions is performed externally and can be implemented in various ways—based on approximate analytical formulations or exact numerical analysis. The frequency domain equivalent currents replacing the transmitting antenna are subsequently modulated by the spectrum of an UWB pulse (in this case, a fourth-order Rayleigh pulse), and their time-domain versions are used as excitation sources in the FDTD time-marching scheme. In the numerical examples presented in sections 3 and 4, the sources are implemented either as an infinitesimal electric dipole, or as uniform electric and magnetic current sheets distributed on a rectangular aperture (the latter approximate the currents produced by a TEM horn antenna, as explained in section 2.3). During the simulation run, the electric fields at the receiving antenna locations are recorded for image generation; specifically, the frequency domain version of the received electric field components is obtained by deconvolving the excitation pulse from the FDTD simulation results.

For sensing applications at low-depression-angles, one salient feature of field interactions in the vicinity of the air/ground interface is the near cancellation of the direct and reflected waves—as it occurs during the illumination of the target by the transmitter, as well as during the propagation of the backscattered target signal to the receiver. Consequently, the direct fields that propagate between closely spaced transmitting and receiving points can be many orders-of-magnitude larger than those received via scattering from the target. As such, to properly characterize the complete field behavior, stringent requirements must be placed on the precision and the dynamic range of the solver to ensure very weak scattering responses are captured. Given these considerations, the only solution for obtaining accurate numerical values of the fields scattered by a target with the “near-field” code is to run the FDTD time-marching process twice—once for the configuration that includes the target and once without the target—and then subtract the received fields from the two cases. The final result is the “perturbation” in the total field introduced by the presence of the target, which is exactly the definition of the scattered field. Note that some types of errors associated with the direct (or “unperturbed”) field are completely cancelled by this procedure. However, other errors, such as numerical dispersion artifacts, cannot be eliminated this way and must be kept under control by choosing a sufficiently-fine grid discretization.

2.5 Time-reversal Imaging With Asymptotics

A coherent field integration technique is employed to process the FDTD-computed scattered signals to obtain an image of the illuminated scene. According to the time-reversal, or phase-conjugation, method, since the received scattered field can be written as

$$E_s = \left(\vec{r}_R, \vec{r}_T, \omega\right) = Y\left(\omega\right) G\left(\vec{r}_s, \vec{r}_T, \omega\right) G\left(\vec{r}_R, \vec{r}_s, \omega\right), \tag{1}$$

an approximate objective (image) function can be formed with the following expression (Borcea et al., 2003; Sarabandi et al., 2004):

$$O = \left(\vec{r}\right) = \sum_{\omega} \sum_{R} \sum_{T} E_s^{*}\left(\vec{r}_R, \vec{r}_T, \omega\right) G\left(\vec{r}, \vec{r}_T, \omega\right) G\left(\vec{r}_R, \vec{r}, \omega\right); \tag{2}$$

where the asterisk notation denotes the phase conjugation operation; $G\left(\vec{r}, \vec{r}', \omega\right)$ is the Green’s function of the environment ($\vec{r}$ is the position of the observation point; $\vec{r}'$ is the position of the source point); $\vec{r}_T, \vec{r}_R,$ and $\vec{r}_s$ are the locations of the transmitter, receiver, and scatterer, respectively; $Y(\omega)$ is the “radiation admittance” of the scatterer—a measure of how easily currents can be induced throughout the object. The cross- and down-range resolution of the image are determined by the sensor aperture and system bandwidth, respectively, of the coherent summation performed in equation 2. For sensing in the presence of a randomly-varying ground interface, as the exact propagation Green's function is not known, $G(\vec{r}, \vec{r}', \omega)$ is approximated by the half-space Green's function; as such, the target image is corrupted by ground clutter.

For the computation of $G(\vec{r}, \vec{r}', \omega)$—or for the characterization of radiation from current sources in the presence of a half-space, note that exact closed-form expressions can be formulated in terms of integrals of the Sommerfeld type; however, these expressions are difficult and time consuming to evaluate numerically (especially when the source and observation points are far apart). To completely avoid the use of Sommerfeld integrals, the transformation of these integrals into asymptotic forms can be carried out by applying the method of steepest descents (Liao and Sarabandi, 2005). The generalized asymptotic expressions—simplified to the half-space propagation scenario—from the work of Liao (2009) are employed here in equation 2 to achieve a more efficient imaging process.

3. Validation of FDTD Solver

The accuracy of the simulation approach outlined in section 2 is determined by comparing FDTD-derived results with those obtained using another full-wave technique, namely, MoM, as implemented in the commercially available electromagnetic software FEKO. Only relatively simple canonical problems are considered in the validation process here, since more complicated scenarios become intractable in FEKO.

The images generated from FDTD- and MoM-computed scattering responses for an on-surface target are compared in figures 2 and 3. A small perfectly conducting cube (side length=88 mm) is considered in figure 2, while a perfectly conducting cylinder (radius=height=15 cm) is considered in figure 3. The antenna source is an infinitesimal electric dipole (vertically-polarized) located above the ground at 2 m height; 16 evenly spaced receiving points are distributed over a 2-m-wide aperture parallel to the *y*-axis with the receiving aperture centered immediately below the dipole, at a height of 1.9 m. The targets are positioned at a down-range distance of either 3.24 m or 18.24 m from the source.

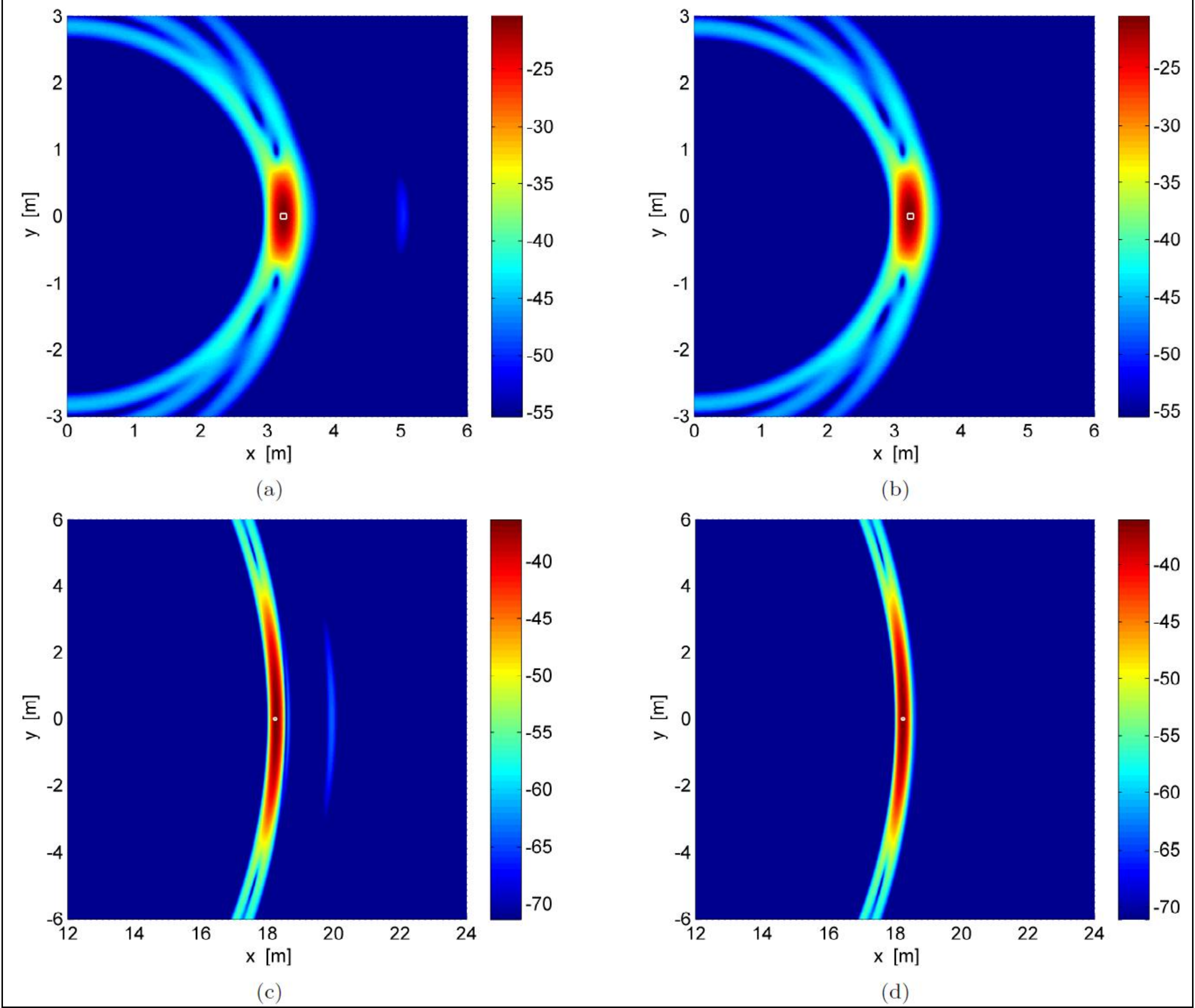

(a) (b) (c) (d)

Figure 2. Comparison of FDTD- and MoM-simulated imaging results for an on-surface, perfectly-conducting cube at two ranges: (a) FDTD: range=3.24 m; (b) MoM: range=3.24 m; (c) FDTD: range=18.24 m; and (d) MoM: range=18.24 m. Ground properties: ε_r=6, σ_d=10 mS/m. Frequency span: 0.1–1.4 GHz.

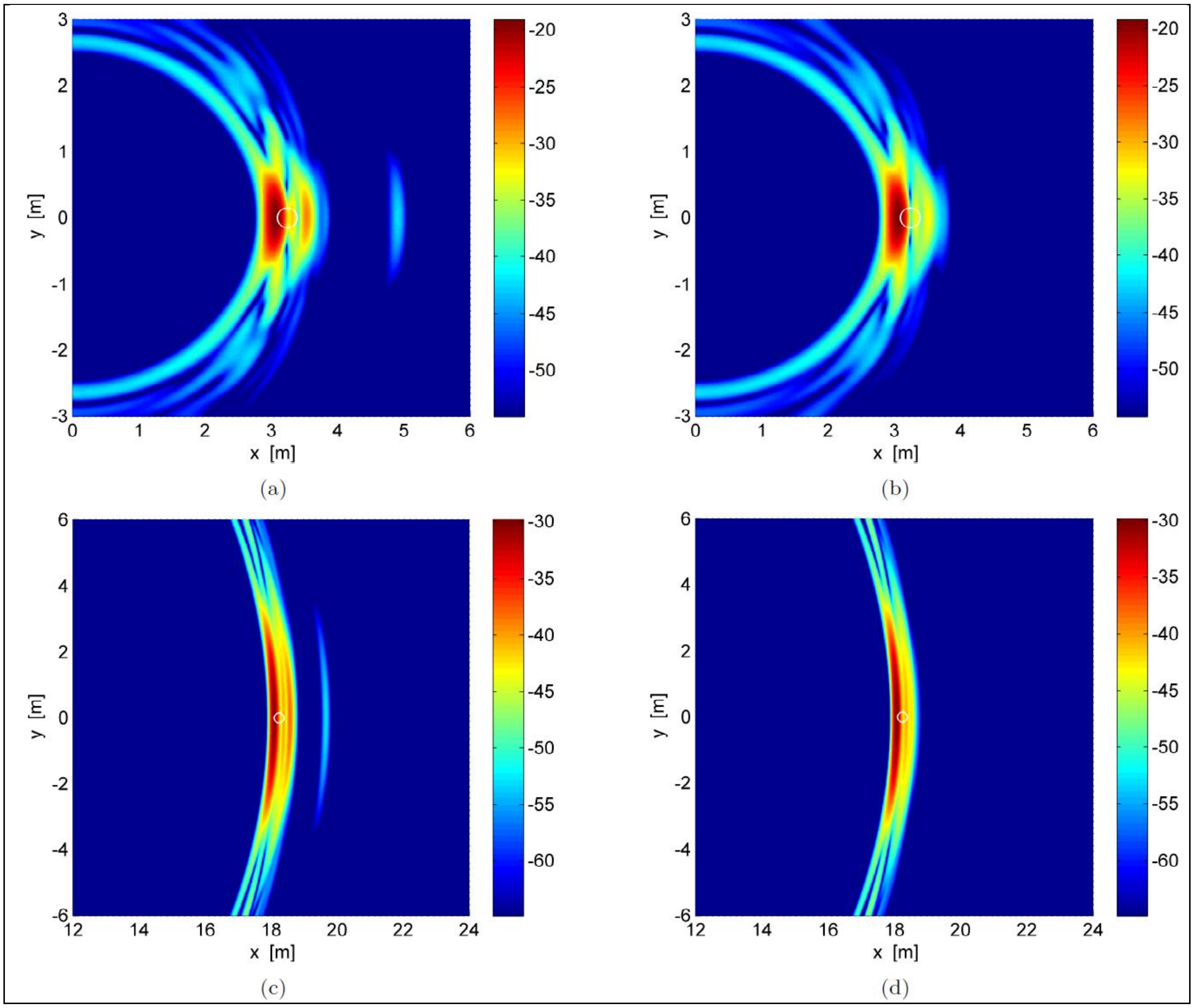

(a)

(b)

(c)

(d)

Figure 3. Comparison of FDTD- and MoM-simulated imaging results for an on-surface, perfectly-conducting cylinder at two ranges: (a) FDTD: range=3.24 m; (b) MoM: range=3.24 m; (c) FDTD: range=18.24 m; and (d) MoM: range=18.24 m. Ground properties: ε_r=6, σ_d=10 *mS/m*. Frequency span: 0.1–1.4 GHz.

As conveyed in the figures, the FDTD results are in good agreement with those from MoM in characterizing the primary return from the target for all test cases analyzed. Unfortunately, the FDTD response contains a late-time return (secondary "echo") that does not appear in the MoM solution. It is conjectured here that this late-time "echo," which lies 23 to 30 dB below the main response, is purely an FDTD simulation artifact—a byproduct of numerical dispersion inherent in FDTD and of the imperfectness of the absorbing boundary condition. It is also observed that the magnitude of this error can be reduced by decreasing the grid cell size. This has to be done, of course, at the expense of increasing the central processing unit (CPU) and memory usage.

4. Large-scale Simulation and Imaging Results

Ful1-wave characterization of the scene shown in figure 1 is performed with the “near-field” FDTD algorithm described in section 2. The computational domain has dimensions of 20 m × 10 m × 4 m and is discretized into 2.6 billion FDTD cells. Parallelized simulations are performed after partitioning the scene into 128 sub-domains (i.e., a total of 128 processors are employed in the MPI network). Approximately 1,000 CPU-hours are needed for each simulation run. As mentioned in section 2.4, the computation of the scattered field essentially requires two runs: one for the “unperturbed” problem—the source in the presence of the flat ground only, without targets—and one for the “perturbed” problem—with targets and any ground-surface roughness. In view of the fact that the SIRE system employs two transmitters, two separate sets of scattering responses (corresponding to two sources of excitation) are synthesized together to form the image for the scene—that is, the transmitters are excited sequentially, not simultaneously, for each simulation.

The effects of a rough ground-surface on focusing are demonstrated with the simulation results displayed in figures 4 and 5, which show the co-polarization images of the scene for different degrees of surface roughness: (a) flat ground; (b) h_{rms}=1.2 cm, l_c=14.93 cm; and (c) h_{rms}=1.6 cm, l_c=14.93 cm. It should be emphasized that the incident (direct) field amplitude at the location of each image pixel, as well as the propagation distance from the pixel to the receiver have been taken into account in the imaging process. In effect, each derived image can be interpreted to be a map containing the spatial variation of the average bi-static radar cross section (RCS) $\bar{\sigma}(\vec{r}_s)$ for the scene, in which the averaging operation is carried over multiple transmitter/receiver locations and a range of frequencies. Consequently, consistent with this RCS interpretation of the observed image intensities, a particular scatterer would appear brighter the closer it is to the radar—due to illumination at a larger depression angle (i.e., away from grazing-angle) that occurs in the near-range. (Depending on the “normalization” method used, the image can also be construed as a map of the electric surface and volumetric current densities induced throughout the scene by the source; this is realized by noting that the term $Y(\omega)G(\vec{r}_s,\vec{r}_T,\omega)$ in equation 1 is basically a transformation of the incident fields into currents.) From the analysis of the point-spread function (see the appendix), note that the sensing resolution for the current setup is $c/2\Delta f$ in the down-range direction and $\lambda_c r/L_{eff}$ in the cross-range direction, where c denotes the speed of light; Δf is the frequency bandwidth; λ_c is the wavelength at the center frequency; r is the range distance; and L_{eff} is the effective aperture length—in this case, it is the sum of the lengths of the transmitting and receiving apertures.

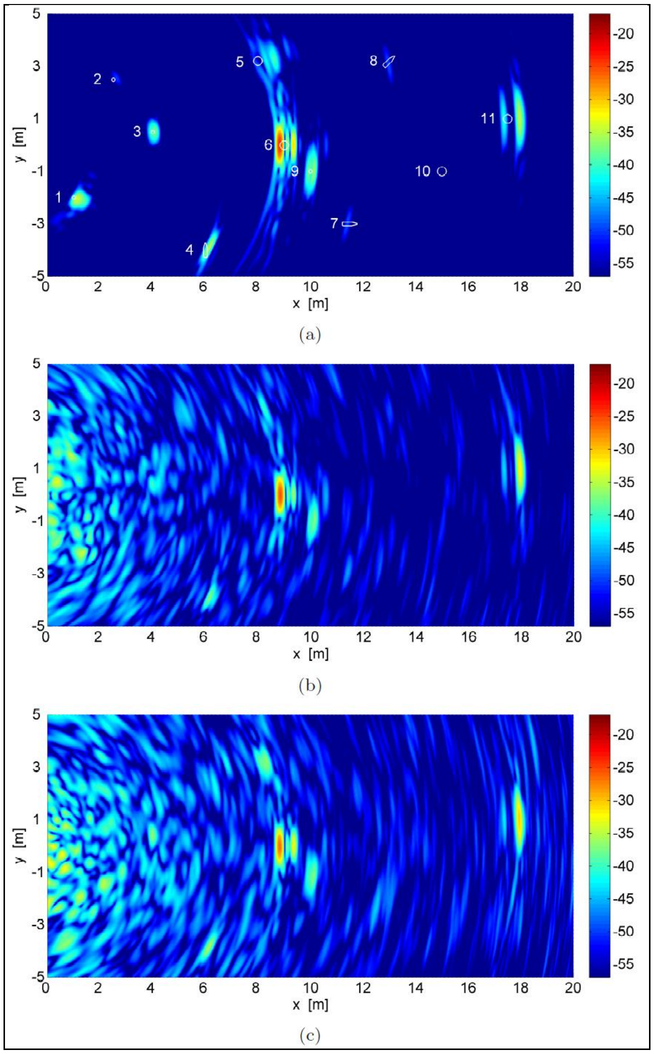

(a)

(b)

(c)

Figure 4. Simulated vertical-vertical (*vv*)-polarized images for 20 m×10 m scene: (a) Ground with flat surface; (b) Ground with randomly rough surface, h_{rms}=1.2 cm, l_c=14.93 cm; (c) Ground with randomly rough surface, h_{rms}=1.6 cm, l_c=14.93 cm. Ground electrical properties: ε_r=6, σ_d=10 *mS*/*m*. Frequency span: 0.3–1.5 GHz.

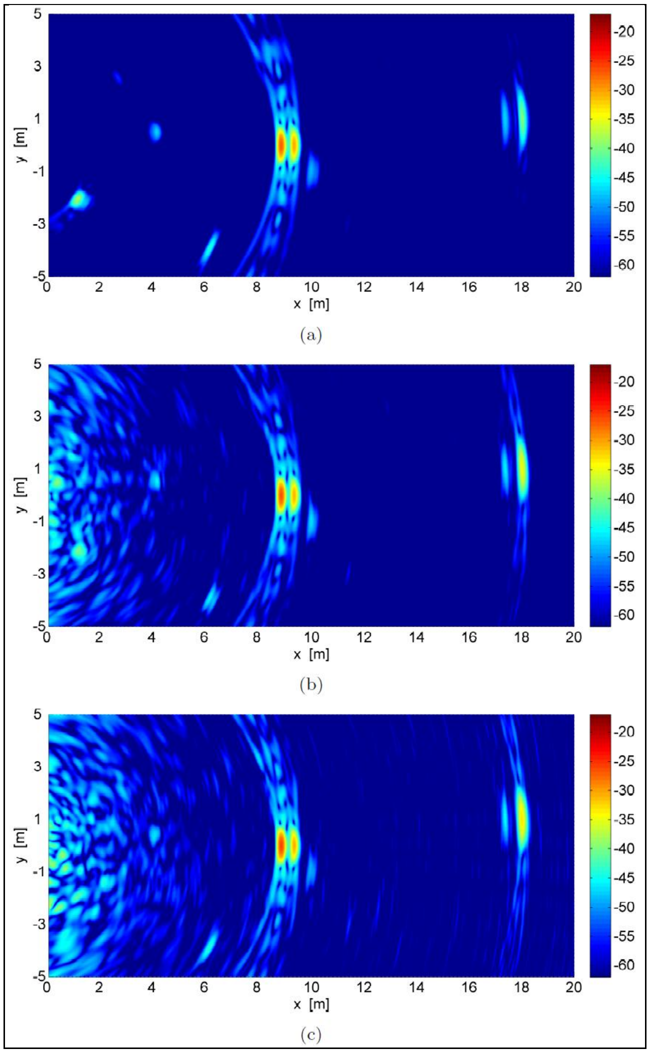

Figure 5. Simulated horizontal-horizontal *(hh)*-polarized images for 20 m×10 m scene: (a) Ground with flat surface; (b) Ground with randomly rough surface, h_{rms} =1.2 cm, l_c=14.93 cm; (c) Ground with randomly rough surface, h_{rms}=1.6 cm, l_c=14.93 cm. Ground electrical properties: ε_r=6, σ_d=10 *mS/m*. Frequency span: 0.3–1.5 GHz.

As seen in the figures, buried targets are generally more difficult to discern from the background as compared to on-surface targets. The response from the larger targets (anti-tank landmines) in the backscattering directions is primarily due to edge-scattering from the front- and back-rims of the top of the cylindrical structure; the scattering centers corresponding to these two edges are resolved in the images—for both on-surface and buried cases. For the smaller targets (anti-personnel landmines), the two scattering-edges tend to merge into one, since the imaging configuration as chosen here is unable to provide sufficient resolution to separate the two phase centers. In the presence of a rough ground interface, these scattering effects are less apparent in the images for the buried targets due to interference from surface scattering. A buried plastic target (either large or small landmine) is especially hard to detect, owing to the limited dielectric contrast between the target and the soil background. (The FDTD artifact discussed in section 3 can also be seen in these images, when its intensity falls within the dynamic range shown—which is true for targets 5 and 6 at *vv*, for example.) The backscattering return from the ground-surface itself is stronger at *vv* than *hh*, and the response at both polarizations tends to decrease as the incidence angle approaches grazing. These observations are consistent with previously reported results derived from far-field simulations (Liao and Dogaru, 2011b) and scatterometer measurements (Oh et al., 1992).

Comparing all target responses across the two polarizations, on average, *vv* provides the stronger return, and it exceeds *hh* by about 5 to 10 dB. As a vertically polarized signal experiences less transmission loss at the air-ground interface and suffers less propagation loss in general, the above observation supports the notion that *vv* is the more desirable configuration for detecting targets either on top of or buried under a flat ground—at the low-frequency region studied (<1.5 GHz). In the presence of ground-surface roughness, detection performance must be evaluated with a consideration of the target-to-background clutter ratio. As such, based on the results of these figures, given that the surface response appears as a stronger interference component at *vv*, it is not apparent that sensing with vertically-polarized waves provides a definitive advantage—for the set of parameters examined herein. The statistical distribution of the ground polarimetric scattering response as a function of the surface properties can also be estimated to facilitate a more comprehensive analysis of the target detection performance.

5. Conclusion

To predict the performance of forward-looking radar technology deployed in complex environments, large-scale, full-wave analysis of multi-static target-imaging in a rough-ground environment is described. The emulation methodology employs a parallelized three-dimensional "near-field" FDTD algorithm in characterizing the electromagnetic scattering from the ground-surface and buried and on-surface targets. The transmitting antennas are represented by equivalent current sheets placed at the real antenna aperture locations. Subsequent focusing of the scattered fields at the receiver locations into an image is obtained by exploiting the time-reversal technique, with the aid of asymptotics. The overall simulator is expected to be a useful tool for studying the effects of ground properties—both physical and electrical—on the signatures of various targets.

As evident from the simulation-based validation studies, the primary scattering returns of the targets are accurately characterized by the proposed FDTD approach; however, numerical artifacts—which manifest as "echoes" of the main imaging response—are also observed. Future work includes investigating the fundamental causes of this error component as well as exploring means to mitigate its effects without compromising the computational efficiency of the solver. Efforts in extending the algorithm to accommodate the full models of the transmitting and receiving antennas will also be undertaken. In addition, multi-aperture scattering and imaging simulations will be performed in the next phase of the study to provide a true emulation of the forward-motion-based operational capability of the SIRE system.

6. References

Altuncu, Y.; Yapar, A.; Akduman, I. On the Scattering of Electromagnetic Waves by Bodies Buried in a Half-Space with Locally Rough Interface. *IEEE Trans. Geosci. Remote Sensing* **2006**, *44* (6), 1435–1443.

Borcea, L.; Papanicolaou, G.; Tsogka, C. A Resolution Study for Imaging and Time Reversal in Random Media. *Cont. Mathem.* **2003**, *313*, 63–67.

Bourgeois, J. M.; Smith, G. S. A Fully Three-Dimensional Simulation of a Ground-Penetrating Radar: FDTD Theory Compared with Experiment. *IEEE Trans. Geosci. Remote Sensing* **1996**, *34* (1), 36–44.

Bourgeois, J. M.; Smith, G. S. A Complete Electromagnetic Simulation of the Separated-Aperture Sensor for Detecting Buried Land Mines. *IEEE Trans. Antennas Propagat.* **1998**, *40* (*10*), 1419–1426.

Bradley, M.; Witten, T.; Duncan, M.; McCummins, B. Mine Detection with a Forward-Looking Ground-Penetrating Synthetic Aperture Radar. *Proc. SPIE*, 2003.

Dobson, M. C.; Ulaby, F. T.; Hallikaiken, M. T.; El-Rayes, M. A. Microwave Dielectric Behavior of Wet Soil—Part II: Dielectric Mixing Models. *IEEE Trans. Geosci. Remote Sensing* **1985**, *23*, 35–46.

El-Shenawee, M.; Rappaport, C. Monte Carlo Simulations for Clutter Statistics in Minefields: AP-Mine-Like-Target Buried Near a Dielectric Object Beneath 2-D Random Rough Ground-Surfaces. *IEEE Trans. Geosci. Remote Sensing* **2002**, *40* (6), 1416–1426.

El-Shenawee, M.; Rappaport, C.; Miller, E. L.; Silevitch, M. B. Three-Dimensional Subsurface Analysis of Electromagnetic Scattering From Penetrable/PEC Objects Buried Under Rough Surfaces: Use of the Steepest Descent Fast Multipole Method. *IEEE Trans. Geosci. Remote Sensing* **2001a**, *39* (6), 1174–1182.

El-Shenawee, M.; Rappaport, C.; Silevitch, M. Monte Carlo Simulations of Electromagnetic Wave Scattering from a Random Rough Surface with Three-Dimensional Penetrable Buried Object: Mine Detection Application Using the Steepest-Descent Fast Multipole Method. *J. Opt. Soc. Am. A* **2001b**, *18*, 3077–3084.

Guan, B.; Zhang, J. F.; Zhou, X. Y.; Cui, T. J. Electromagnetic Scattering From Objects Above a Rough Surface Using the Method of Moments with Half-Space Green's Function. *IEEE Trans. Geosci. Remote Sensing* **2009**, *47* (10), 3399–3405.

Gürel, L.; Oğuz, U. Three-Dimensional FDTD Modeling of a Ground-Penetrating Radar. *IEEE Trans. Geosci. Remote Sensing* **2000**, *38* (4), 1513–1521.

Gürel, L.; Oğuz, U. Simulations of Ground-Penetrating Radars Over Lossy and Heterogeneous Grounds. *IEEE Trans. Geosci. Remote Sensing* **2001**, *39* (6), 1190–1197.

He, J.; Yu, T.; Geng, N.; Carin, L. Method of Moments Analysis of Electromagnetic Scattering From a General Three-Dimensional Dielectric Target Embedded in a Multilayered Medium. *Radio Sci.* **2000**, *35* (2), 305–313.

Johnson, J. T. A Numerical Study of Scattering from an Object Above a Rough Surface. *IEEE Trans. Antennas Propagat.* **2002**, *50* (10), 1361–1367.

Johnson, J. T.; Burkholder, R. J. Coupled Canonical Grid/Discrete Dipole Approach for Computing Scattering From Objects Above or Below a Rough Interface. *IEEE Trans. Geosci. Remote Sensing* **2001**, *39* (6), 1214–1220.

Kositsky, J.; Cosgrove, R.; Amazeen, C.; Milanfar, P. Results from a Forward-Looking GPR Mine Detection System. *Proc. SPIE*, 2002.

Lampe, B.; Holliger, K. Numerical Modeling of a Complete Ground-Penetrating Radar System. *Proc. SPIE*, 4491, 2001.

Liao, D. H. *Physics-Based Near-Earth Radiowave Propagation Modeling and Simulation*, Ph.D. Thesis, The University of Michigan, 2009.

Liao, D. H. *Full-Wave Characterization of Rough Terrain Surface Effects for Forward-Looking Radar Applications: A Scattering and Imaging Study From the Electromagnetic Perspective*; ARL-TR-5758; U.S. Army Research Laboratory: Adelphi, MD, 2011.

Liao, D. H.; Dogaru, T. Full-Wave-Based Emulation of Forward-Looking Radar Target Imaging in Rough Terrain Environment. *Proc. IEEE Antennas and Propagat. Soc. Sym.*, 2011a.

Liao, D. H.; Dogaru, T. A Comparison of Surface Integral Equation and FDTD Methods for Modeling Backscattering From Dielectric Rough Surfaces at Near-Grazing-Angles. *Proc. IEEE Antennas and Propagat. Soc. Sym.*, 2011b.

Liao, D. H.; Dogaru, T. Full-Wave Characterization of Rough Terrain Surface Scattering for Forward-Looking Radar Applications. *IEEE Trans. Antennas Propagat.* **2012**, *60* (8), 3853–3866.

Liao, D. H.; Dogaru, T.; Sullivan, A. Characterization of Rough Surface Clutter for Forward-Looking Radar Applications. *Proc. 27th Army Science Conf.*, 2010.

Liao, D. H.; Sarabandi, K. Near-Earth Wave Propagation Characteristics of Electric Dipole in Presence of Vegetation or Snow Layer. *IEEE Trans. Antennas Propagat.* **2005**, *53* (11), 3747–3756.

Oh, Y.; Sarabandi, K.; Ulaby, F. T. An Empirical Model and an Inversion Technique for Radar Scattering from Bare Soil Surfaces. *IEEE Trans. Geosci. Remote Sensing* **1992**, *30*, 370–381.

Peplilnski, N. R.; Ulaby, F. T.; Dobson, M. C. Dielectric Properties of Soils in the 0.3–1.3 GHz Range. *IEEE Trans. Geosci. Remote Sensing* **1995**, *33*, 803–807.

Ressler, M.; Nguyen, L.; Koenig, F.; Wong, D.; Smith, G. The ARL Synchronous Impulse Reconstruction (SIRE) Forward-Looking Radar. *Proc. SPIE*, 2007.

Sarabandi, K.; Koh, I.; Casciato, M. Demonstration of Time Reversal Methods in a Multi-Path Environment. *Proc. IEEE Antennas and Propagat. Soc. Sym.*, 2004.

Taflove, A.; Hagness, S. C. *Computational Electrodynamics: The Finite-Difference Time-Domain Method*; Third Edition. Artech House: Boston, MA. 2005.

Teixeira, F. L.; Chew, W. C.; Straka, M.; Oristaglio, M. L.; Wang, T. Finite-Difference Time-Domain Simulation of Ground Penetrating Radar on Dispersive, Inhomogeneous, and Conductive Soils. *IEEE Trans. Antennas Propagat.* **1998**, *36* (6), 1928–1937.

Thorsos, E. I. The Validity of the Kirchhoff Approximation for Rough Surface Scattering Using a Gaussian Roughness Spectrum. *J. Acoust. Soc. Am.* **1988**, *83*, 78–92.

Uduwawala, D.; Norgren, M.; Fuks, P. A Complete FDTD Simulation of a Real GPR Antenna System Operating Above Lossy and Dispersive Grounds. *Progress in EM Res.* **2005**, *50*, 209–229.

Wang, J.; Li, Y.; Zhou, Z.; Jin, T.; Yang, Y.; Wang, Y. Image Formation Techniques for Vehicle-Mounted Forward-Looking Ground-Penetrating SAR. *Proc. SPIE*, 2008.

Wang, T.; Sjahputera, O.; Keller, J. M. Landmine Detection Using Forward-Looking GPR With Object Tracking. *Proc. SPIE*, 2005.

Wang, X.; Wang, C.-F.; Gan, Y.-B. Electromagnetic Scattering From A Circular Target Above Or Below Rough Surface. *Progress in EM Res.* **2003**, *40*, 207–227.

Zhuge, X.; Yarovoy, A. G. A Sparse Aperture MIMO-SAR-Based UWB Imaging System for Concealed Weapon Detection. *IEEE Trans. Geosci. Remote Sensing* **2011**, *49*, 509–518.

INTENTIONALLY LEFT BLANK.

Appendix. Derivation of the Imaging Point-Spread Function

Consider an array of vertically polarized point radiators and a point-scatterer directly on the ground at $\vec{r}_s = (r_s, \theta_s, \phi_s)$, approximating the Green's function for the interactions of the co-polarized field component as (Liao, 2009)

$$G(\vec{r}, \vec{r}', k) \propto e^{-ik|\vec{r}-\vec{r}'|} \left\{ \frac{1}{|\vec{\rho}|} + \frac{R(\theta_{illu})}{|\vec{\rho}|} + \frac{C_1}{|\vec{\rho}|^2} + \frac{C_2}{|\vec{\rho}|^3} + \cdots \right\} = e^{-ik|\vec{r}-\vec{r}'|} F(\vec{r}, \vec{r}'), \tag{A-1}$$

and assuming observation with an array of isotropic point receivers, the point-spread function (PSF) can be constructed from equation 2 as

$$PSF(\vec{r}, \vec{r}_s) \approx \sum_{k} \sum_{L_R} \sum_{L_T} e^{ik|\vec{r}_s - \vec{r}_T|} F(\vec{r}_s, \vec{r}_T) e^{ik|\vec{r}_R - \vec{r}_s|} F(\vec{r}_R, \vec{r}_s) e^{-ik|\vec{r}-\vec{r}_T|} F(\vec{r}, \vec{r}_T) e^{-ik|\vec{r}_R - \vec{r}|} F(\vec{r}_R, \vec{r}). \tag{A-2}$$

Using far-field expressions for the distance vectors, the $F(\cdot)$ terms can be moved outside the summation operation, and orienting the transmitting and receiving arrays parallel to the y-axis ($x_R = x_T = 0$), the function in equation A-2—on the xy-plane—becomes

$$PSF(\vec{r}, \vec{r}_s) \propto F(\vec{r}_s, \vec{r}_T) F(\vec{r}_R, \vec{r}_s) F(\vec{r}, \vec{r}_T) F(\vec{r}_R, \vec{r}). \\ \sum_{n_k} \sum_{n_R} \sum_{n_T} e^{2in_k \delta k (r_s - r)} e^{i(n_k \delta k + k_c) n_R \delta y_R (\sin\phi - \sin\phi_s)} e^{i(n_k \delta k + k_c) n_T \delta y_T (\sin\phi - \sin\phi_s)}, \tag{A-3}$$

where δk, δy_R, and δy_T are the k-space sampling interval, the receiver spacing, and the transmitter spacing, respectively; k_c is the center wavenumber; the wavenumber bandwidth is $\Delta k = N_k \delta k$; and the aperture sizes are $L_R = N_R \delta y_R$, and $L_T = N_T \delta y_T$. Applying a stationary-phase-like approach to evaluate the summation in k-space and noting the relation

$$\left| \sum_{n=0}^{N-1} e^{-inu} \right| = \left| \frac{\sin\left(\frac{Nu}{2}\right)}{\sin\left(\frac{u}{2}\right)} \right|, \tag{A-4}$$

the amplitude of equation A-3 approximately simplifies to

$$|PSF(\vec{r}, \vec{r}_s)| \propto |F(\vec{r}_s, \vec{r}_T) F(\vec{r}_R, \vec{r}_s) F(\vec{r}, \vec{r}_T) F(\vec{r}_R, \vec{r})|. \\ \left| \frac{\sin(\Delta k (r_s - r))}{\sin(\delta k (r_s - r))} \cdot \frac{\sin\left(\frac{L_R k_c (\sin\phi - \sin\phi_s)}{2}\right)}{\sin\left(\frac{\delta y_R k_c (\sin\phi - \sin\phi_s)}{2}\right)} \cdot \cos\left(\frac{L_T k_c (\sin\phi - \sin\phi_s)}{2}\right) \right|, \tag{A-5}$$

where it is assumed that there is a transmitter at each end of the aperture L_T. The first sin $(\cdot)$ / sin $(\cdot)$ term in equation A-5 dictates the behavior of the PSF in range: it can be shown that the first null occurs at $c/2\Delta f$—which is the resolution in range, δr, independent of r_s and ϕ_s. The periodicity of this term determines the frequency sampling interval needed: for maximum-range $r_{s,max}$, the condition $\delta f < c/2r_{s,max}$ must be met. Similarly, the cross-range properties of the PSF are controlled by the last two terms in equation A-5. For the current two-transmitter system (and $L=L_T=L_R$), based on the location of the first null of these two terms, it can be readily seen that the angular resolution depends on the angular position of the scatterer as

$$\delta\phi = \phi_s - \sin^{-1}\left(\sin\phi_s - \frac{\lambda_c}{2L}\right), \quad 0 \le \phi_s < \frac{\pi}{2}. \tag{A-6}$$

At $\phi_s=0$, $\delta\phi \approx \lambda_c/2L$; the angular resolution degrades as the scatterer moves away from the broadside direction of the aperture. In general, the spatial sampling should be less than $\lambda_{min}/2$; however, for an UWB system, it has been shown (Zhuge and Yarovoy, 2011) that high cross-range resolution can be achieved with coarser sampling than the stated criterion.

List of Symbols, Abbreviations, and Acronyms

ARL	U.S. Army Research Laboratory
CPU	central processing unit
FDTD	finite-difference time-domain
GPR	ground-penetrating radar
hh	horizontal-horizontal
IED	improvised explosive devices
MoM	method-of-moments
MPI	message-passing interface
PML	perfectly-matched layer
PSF	point-spread function
RCS	radar cross section
rms	root mean square
SIRE	synchronous impulse reconstruction
TEM	transverse electromagnetic
UWB	ultra-wideband
vv	vertical-vertical

NO. OF COPIES	ORGANIZATION
1	ADMNSTR DEFNS TECHL INFO CTR ATTN DTIC OCP 8725 JOHN J KINGMAN RD STE 0944 FT BELVOIR VA 22060-6218
9	US ARMY RSRCH LAB ATTN IMAL HRA MAIL & RECORDS MGMT ATTN RDRL CIO LL TECHL LIB ATTN RDRL SER U TRAIAN DOGARU KARL KAPPRA DAHAN LIAO (3 COPIES) ANDY SULLIVAN ADELPHI MD 20783-1197